Electronic Supplementary Information

Synthesis and Application of Hollow Magnetic Graphitic Carbon Microspheres with/without TiO_2 Nanoparticle Layer on the Surface

Shanshan Feng [a], *Zhiyu Ren* [a], *Yuanlong Wei* [b], *Baojiang Jiang* [a], *Yang Liu* [a], *Lingyi Zhang* [b], *Weibing Zhang* [b] *and Honggang Fu* [a]*

[a] Key Laboratory of Functional Inorganic Material Chemistry, Ministry of Education of the People's Republic of China, Heilongjiang University, Harbin 150080 P. R. China

[b] School of Chemistry and Molecular Engineering, East China University of Science and Technology, Shanghai 200237 P. R. China

Corresponding author E-mail: fuhg@vip.sina.com,

Tel.: +86 451 8660 8458,

Fax: +86 451 8667 3647

Experimental

1. Synthesis of hollow magnetic graphitic carbon microspheres (HMGS)

0.8 g of *β*-CD was dissolved in 48 mL of H_2O with stirring, and then 4.8 mL of aqueous solution containing Fe_3O_4 NPs stabilized by OA and ammonia (10 g L^{-1}) were added.[1] The resulting solution was transferred into a Teflon-lined stainless autoclave and was kept in oven at 160 ℃, 170 ℃, 175 ℃, 180 ℃ and 190 ℃ for 24 h, respectively. After cooling down naturally, the final products washed thoroughly with deionized water and ethanol. The HMCSs were obtained. For further carbonization, as-prepared HMCSs were calcined under high-purity nitrogen stream at 700 ℃ for 2 h with a temperature ramp of 10 ℃ min^{-1}.

2. Synthesis of HMGS@TiO_2 microspheres

8.5 mL of tetrabutyltitanate (TBT) was dissolved in 40 mL of mixture solution containing ethanol and ethanolamine under stirring, followed by dropwise additon of a mixture solution of water and ethanol (1:5, v/v). After stirring for 2 h, 100 mg of as-prepared HMCSs were dispersed in the above solution. The HMCSs decorated with TBT were separated and washed with ethanol. After dried in vacuum, the obtained powder was calcined under high-purity nitrogen stream at 700 ℃ for 2 h with a temperature ramp of 10 ℃ min^{-1}.

3. Enrichment of Phosphopeptides by HMGS@TiO_2 microspheres

In brief, a suspension of HMGS@TiO_2 microspheres (20 mg mL^{-1}) was prepared by dispersing in 50% ACN and 0.1% TFA aqueous solution (v/v). After incubation for 30 min, 5 μL of the suspension was added into peptide mixture (200 μL, 1×10^{-7} mol L^{-1}) originating from tryptic digestions, and the mixed solutions were vibrated for 30 s. After that, with the help of magnet, the peptides-HMGS@TiO_2 microspheres were collected by removal of the supernatant and rinsed with 50% ACN and 0.1% TFA aqueous solution (v/v) for two times. Then, the obtained peptide-loaded HMGS@TiO_2 microspheres were re-dispersed in 10 μL of 50% ACN aqueous solution (v/v).

Characterization

SEM images and EDX spectrum were recorded with a Hitachi S-4800 field emission scanning electron microscope. TEM images were taken with a JEM-3010 electron microscope (JEOL, Japan). FT-IR spectra were recorded on a Nicolet IS10. XRD pattern was performed on Rigaku D/max-IIIB. XPS spectrum was recorded with PHI 5700. Raman spectra were performed on a Jobin Yvon HR 800 micro-Raman spectrometer at 457.9 nm. Hysteresis loop of the sample was obtained using a vibrating sample magnetometer (VSM) (model 730, Lakeshore). The heavy metal ions concentration was measured by atomic absorption spectrometry (AAS, Thermo Elemental SOLAAR-M). The MALDI-TOFMS analyses were performed in positive ion mode on Voyager-DE STR mass spectrometer (Applied Biosystems, Framingham, MA, USA)

Results and discussion

1 Fe_3O_4 nanoparticles (NPs) stabilized by oil acid (OA) and ammonia

Pure phase Fe_3O_4 NPs were prepared by coprecipitation (as shown in Fig. S1),[1] which were further stabilized by OA and ammonia. The position of the XRD peaks at 2θ = 30.2°, 35.3°, 43.2°, 57.5° and 62.9° are ascribed to the diffraction of the face-centered cubic (fcc) structure of Fe_3O_4 respectively.

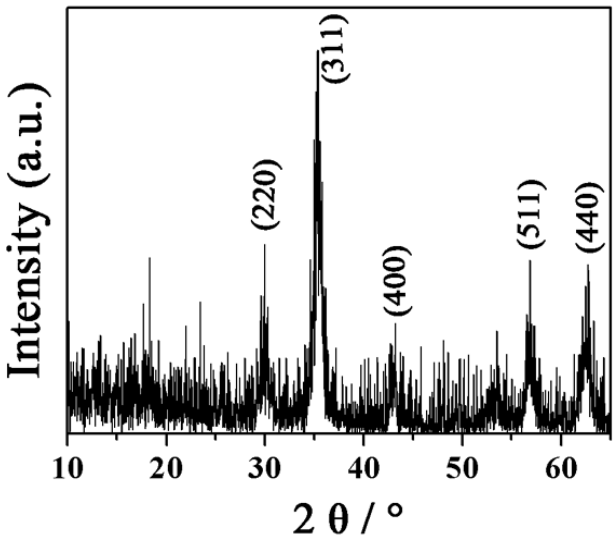

Fig. S1 XRD spectra of the as-prepared Fe_3O_4 NPs.

The FT-IR spectra of OA (a), Fe_3O_4 NPs modified by OA (b) and Fe_3O_4 NPs stabilized by OA and ammonia (c) are presented in Fig. S2. The assignment of the characteristic FT-IR absorption bands are summarized in Table S1. Compared the FT-IR spectra of Fe_3O_4 NPs modified by OA with that of OA, a new absorption speak at 1585 cm^{-1} corresponds to the free $-COO^-$ group, implying that the existence of free OA. Meanwhile, the characteristic absorption speak of Fe-O bond at 571 cm^{-1} can be observed indicating that the presence of Fe_3O_4 NPs. When ammonia is introduced to this system, significant changes appear in the FT-IR spectra. Accompanied with the disappearance of absorption speak of OA dimer at 1710 cm^{-1} (ν (C=O)), a stronger and broader absorption band at 1623 cm^{-1} exhibit in the FT-IR spectra of Fe_3O_4 NPs stabilized by OA and ammonia, which involves the absorption bands of ν_{as} (NH_4^+), ν_s (C-H) and the free $-COO^-$ group. The strong speak at 1384 cm^{-1} is attributed to the composite absorptions of N-O bonds and δ_s ($-CH_3$). Moreover, the absorption band from 3500-2800 cm^{-1} is broadened due to the composite of ν (N-H), ν (C-H) and ν (O-H). The results imply that Fe_3O_4 NPs are stabilized by OA and ammonia.

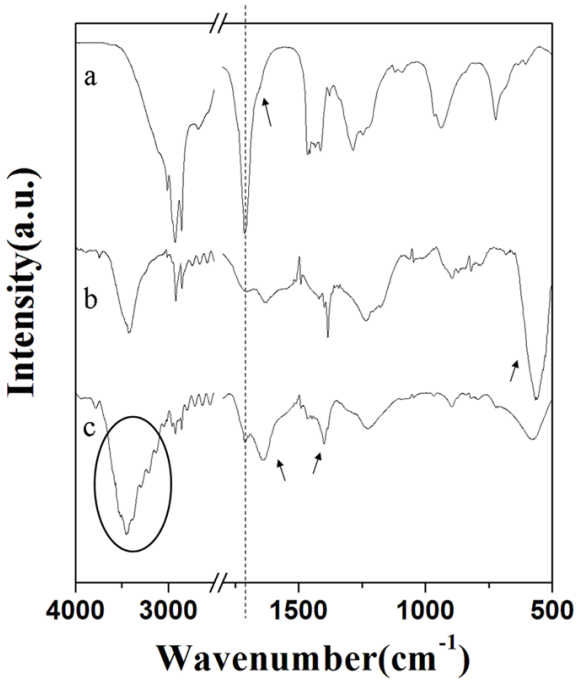

Fig. S2 FT-IR spectra of a) pure OA; b) Fe_3O_4 NPs modified by OA; c) Fe_3O_4 NPs stabilized by OA and ammonia.

Table S1. Assignment of FT-IR spectra of a) pure OA; b) Fe_3O_4 NPs modified by OA; c) Fe_3O_4 NPs stabilized by OA and ammonia (presented in Fig. S2).

samples	IR absorption bands/cm^{-1}	description
a	3009	ν (=C-H)
	2924，2855	ν_{as} (CH_2), ν_s (CH_2)
	1713	ν (C=O) : dimer of OA
	1285	ν (C-O) , ν (C-H)
b	3650-3200	ν (O-H),
	571	absorption bands of the Fe-O bond
c	3500-2800	ν (N-H), ν (C-H) , ν(O-H)
	1623	ν_{as} (NH_4^+), ν_s (C-H)
	1384	N-O and δ_s (-CH_3)

ν_s, symmetric stretching vibration; ν_{as}, asymmetric stretching vibration; δ, bending vibration

2 Fe_3O_4 NPs modified by β-cyclodextrins (Fe_3O_4/β-CD)

Compared the FT-IR spectra of Fe_3O_4/β-CD with that of Fe_3O_4 NPs stabilized by OA and ammonia, a series of characteristic absorption bands of β-CD appear in the spectra of Fe_3O_4/β-CD. The bands (1025-1157 cm^{-1}) assigned to the antisymmetric glycosidic vibrations of ν_a (C-O-C) and the coupled ν (C-C/CO) stretch vibration.[2, 3] The peaks in the range of 1299-1460 cm^{-1} attributed to the composite of the deformation vibrations of σ (C-H) and σ (O-H) of the CH_2 and OH groups. Meanwhile, the characteristic peak of the ring vibrations at 945 cm^{-1} also appears. These results provide strong evidence for the presence of the β-CD around the Fe_3O_4 NPs.

In addition, the difference between Fe_3O_4/β-CD and pure β-CD can also be observed in the IR spectra. The peak of Fe_3O_4/β-CD at 2930 cm^{-1} (ν_a (CH_2)) is shifted by ~9 cm^{-1} compared to that in Fe_3O_4 NPs stabilized by OA and ammonia (2921 cm^{-1}). The coupled ν (C-C/C-O) stretch vibration band in sample of Fe_3O_4/β-CD appears at 1029 cm^{-1}, which is blue-shifted by ~5 cm^{-1} compared with the peak of pure β-CD. These results suggest that β-CD may interact with OA.

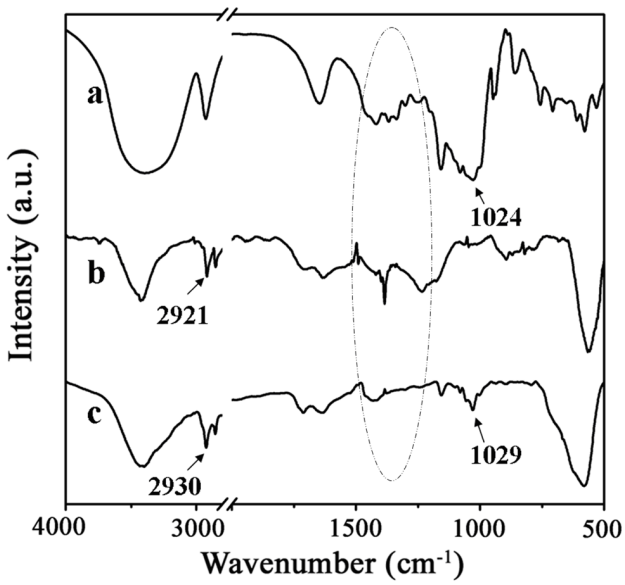

Fig. S3 FT-IR spectra of a) pure *β*-CD; b) Fe_3O_4 NPs stabilized by OA and ammonia; c) Fe_3O_4/*β*-CD.

3 Structural characteristic of HMCSs and HMGSs

3.1 The effect of hydrothermal temperature on the structure of HMCSs

The effect of hydrothermal temperature on the structure of HMCSs was studied as shown in Fig. S4. Obviously, HMCSs cannot form until the hydrothermal temperature reaches 170 ℃. During the hydrothermal reaction, the hydrolyzation, dehydration and carbonization reactions of *β*-CD occur. If the hydrothermal temperature is not high enough to cause the carbonization (below 170 ℃), only the compound of carbon and Fe_3O_4 NPs can be obtained (as shown in Fig. S4A and Fig. S4E). When the hydrothermal temperature meets or exceeds the temperature of carbonization (in the range of 170 ℃-180 ℃), Fe_3O_4/*β*-CD and *β*-CD assemble around the bubbles of NH_3 and be carbonized to form HMCSs. However, it is difficult to control the sizes of cavities and carbon microspheres due to the random sizes of bubbles in the system. However, further increasing the hydrothermal temperature to 190 ℃, lots of solid carbon microspheres besides HMCSs with small hollow cavities emerge. Maybe, the formation of lots of solid carbon microspheres results from the violent and fast reactions of Fe_3O_4/*β*-CD and *β*-CD under the higher hydrothermal temperature. The reactions of

hydrolyzation, dehydration and carbonization of *β*-CD have started before the aggregation and assembly of Fe_3O_4/*β*-CD and *β*-CD around bubbles occur.

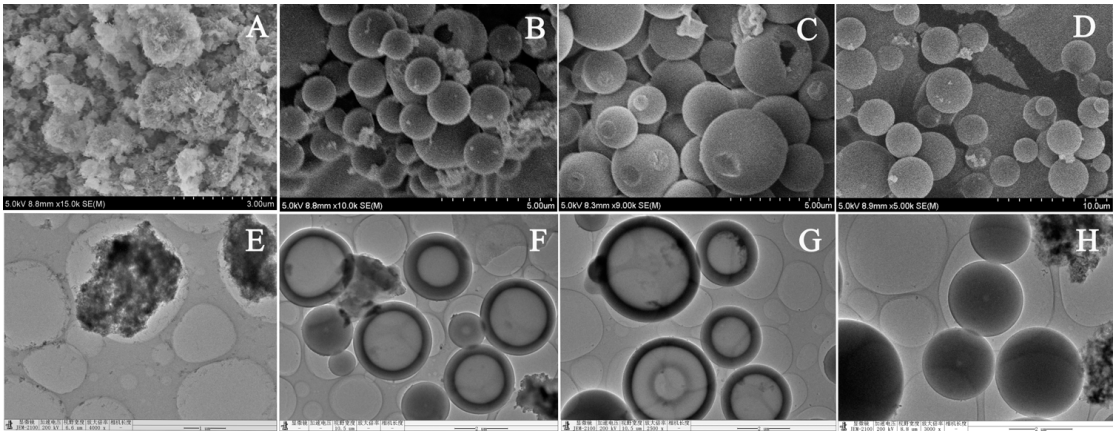

Fig. S4 Typical SEM and TEM images of HMCSs synthesized at different hydrothermal temperatures for 24 h: A, E) 160 ℃; B, F) 170 ℃; C, G) 180 ℃ and D, H) 190 ℃.

3.2 Structural characteristic of HMCSs and HMGSs

The bands at 1700 cm^{-1} and 1620 cm^{-1} attribute to C=O and C=C vibrations, respectively, which attest the carbonization and aromatization during the hydrothermal treatment.[4-6] The bands at 3390 cm^{-1} implies the existence of large numbers of residual hydroxyl groups, implying that it is possible for the loading of other functional molecules to widen applications. Whereas, it is noteworthy that the bands at 575 cm^{-1} exhibit in the FT-IR spectra of as-prepared HMCSs, which attribute to the absorptions band of Fe-O bond of the Fe_3O_4 NPs.[7] The result implies that the assembly under hydrothermal condition involves not only *β*-cyclodextrin (*β*-CD) but also Fe_3O_4 NPs modified by *β*-CD (Fe_3O_4/*β*-CD), which is consistent with our prediction.

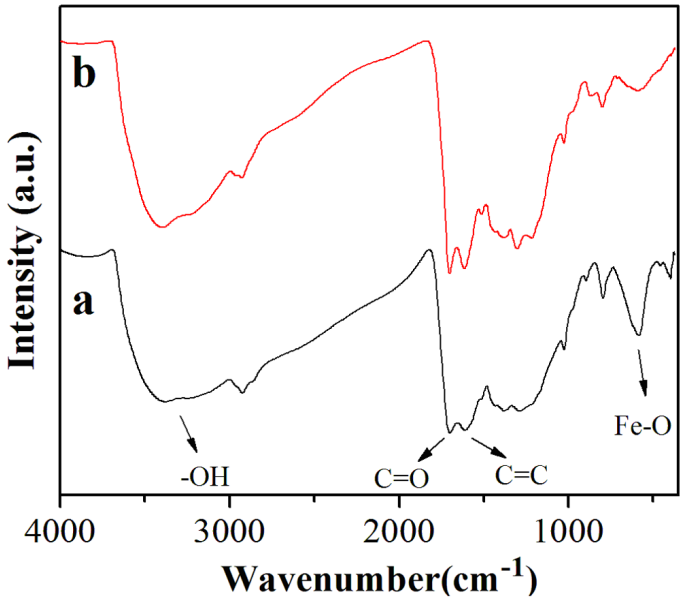

Fig. S5 FT-IR spectra of a) HMCSs prepared by synchronous hydrothermal reaction of *β*-CD and Fe_3O_4/*β*-CD; b) pure *β*-CD.

Herein, to study the pathways for the formation of the graphitic carbon in detail, HMCSs after carbonization at different temperatures were measured by XRD (shown in Fig. S6). From the patterns of XRD, it can be seen that no obvious diffraction peaks of graphite are observed until the temperature reached 700 ℃. Two peaks of XRD pattern at 2θ = 26.26° and 44.38° can be clearly observed, which can be indexed as graphitic (002) and (101) planes, respectively, implying that the conversion of carbon structure from the amorphous carbon to the highly crystallized graphite takes place. The results maybe attributes to the appearance of Fe_2O_3 (at 650 ℃). With the temperature of carbonization increasing, lots of carbon dioxide produces due to the decomposition of organic molecule, which could use as the oxidant to cause the formation of Fe_2O_3 attaching to the surface of Fe_3O_4 NPs. The produced Fe_2O_3 possess catalyze effect to cause the graphitization of amorphous carbon around Fe_2O_3. In contrast, the carbon located far from Fe_2O_3 is not graphitized resulting in the weak diffraction peaks of graphite.

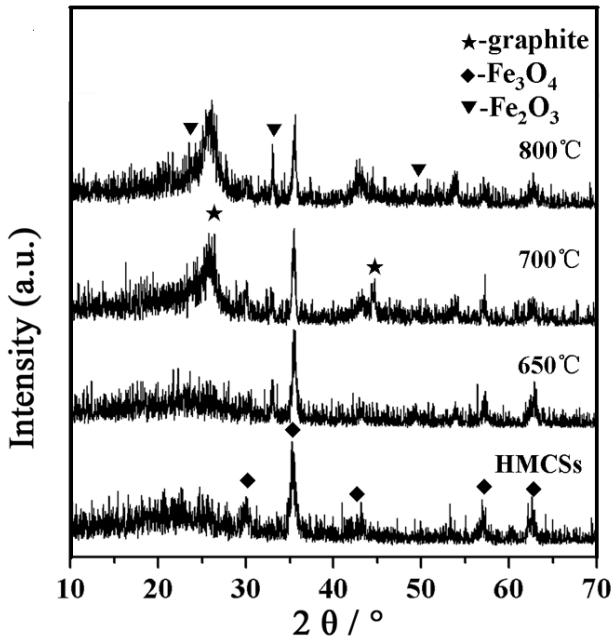

Fig. S6 XRD patterns of HMGSs at different carbonization temperatures.

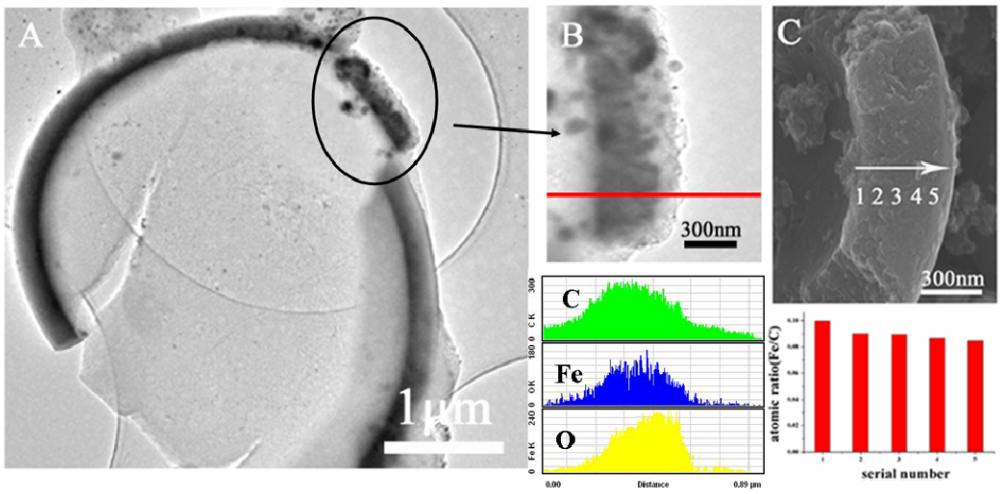

Fig. S7 A) and B) TEM image of triturated HMCSs, and linear scan analysis from the TEM image demonstrating distributing of C, O and Fe elements; C) Typical SEM of triturated HMGSs, and atomic ratio of Fe/C pattern along the arrow.

To further validate the distribution of Fe_3O_4 NPs in HMCSs, XPS spectra of HMCSs were measured. Considering the tiny difference in the atomic ratio of Fe/C, the XPS spectra of the original HMCSs and the triturated HMCSs were measured in experiments, respectively. The concentration of C, O and Fe element were analyzed via the intensity of the peaks (as shown in Fig. S8). The concentration of Fe and O element measured from the triturated HMCSs is a

little higher than that measured from the HMGSs. In contrast, the concentration of C element of the triturated sample decrease compared with that of the original HMCSs. Such result accords with the linear scan analysis from the TEM and SEM images.

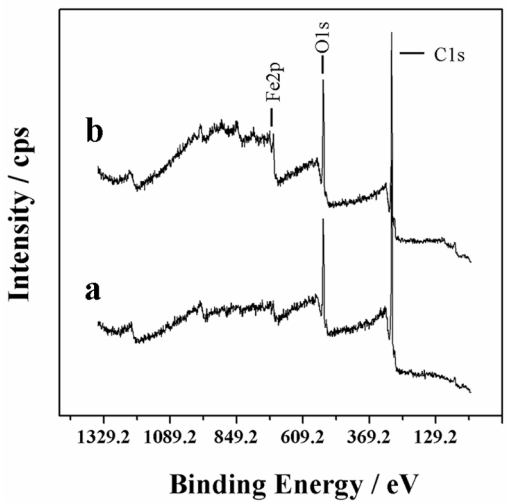

	Element	Area (cts-eV/s)	Sensitivity Factor	Concentration (%)
HMCSs	C1s	6317	6.994	76.38
	O1s	4499	17.428	21.83
	Fe2p	1557	73.679	1.79
triturated HMCSs	C1s	5656	6.994	71.55
	O1s	4752	17.428	24.12
	Fe2p	3600	73.679	4.32

Fig. S8 XPS spectra of the whole HMGSs (a) and the triturated HMGSs (b); and the analysis of the concentration of C, O and Fe element.

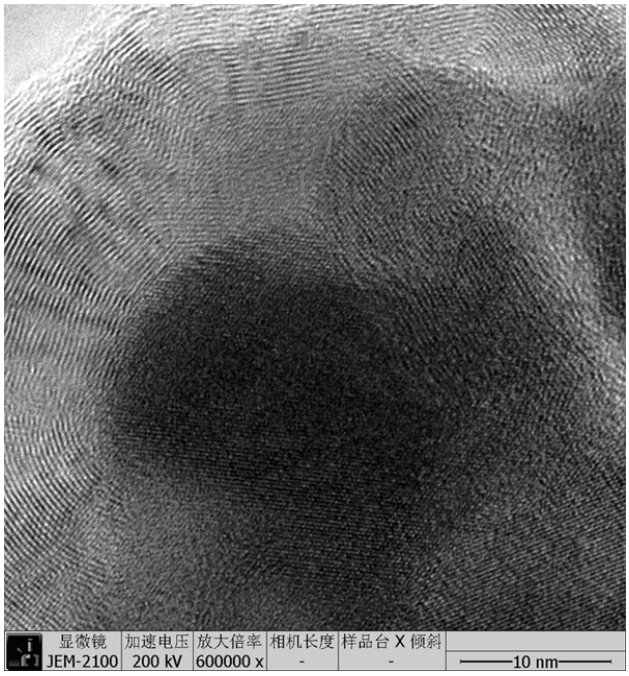

Fig. S9 HRTEM images of HMGSs (the original image of Fig. 1F).

The graphitic carbon structure is also evident in the Raman spectra shown in Fig. S10. Compared with the Raman spectra of HMCSs, the G band at 1587 cm^{-1} arising from in-plane stretching is noticeably sharper and the broad multi-band peaks around 2700 cm^{-1} (2D) are appear, which are consistent with the multi-layer feature of graphite.[8] The strong D band speak at 1341 cm^{-1} can also be observed, which maybe is attributed to the vibration mode of carbon atoms with dangling bonds at the edges of graphite defects and the presence of amorphous carbon in HMGSs.

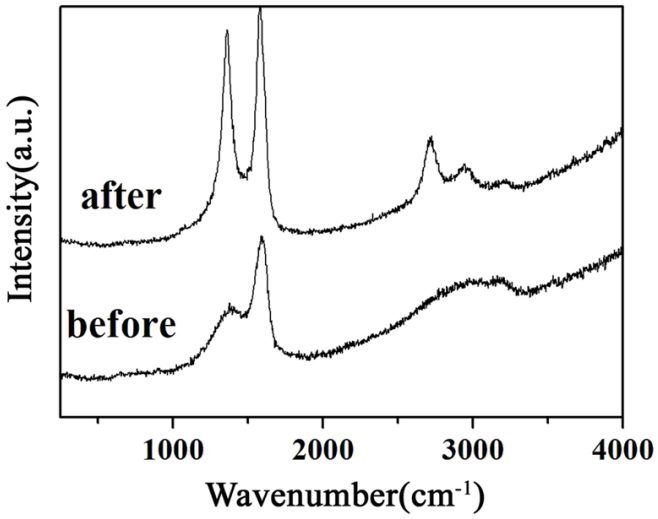

Fig. S10 Raman spectra of HMCSs before and after calcination.

4 Formation mechanisms of HMCSs

4.1 Effect of ammonia on the formation of HMCSs

In experiment, TG coupled with a FT-IR (TG/FT-IR) technique was used to certify the liberation of NH_3 gas from Fe_3O_4 NPs stabilized by OA and ammonia. Compared with standardized spectra of NH_3 gas and water vapour, the evolution of the IR spectra in the region 3400-3200 cm^{-1} and 1200-800 cm^{-1} display that NH_3 gas release gradually with increasing temperature. Moreover, it is noteworthy that the hydrothermal reaction is a close system in which the released NH_3 gas can re-dissolve to form bubble-template.

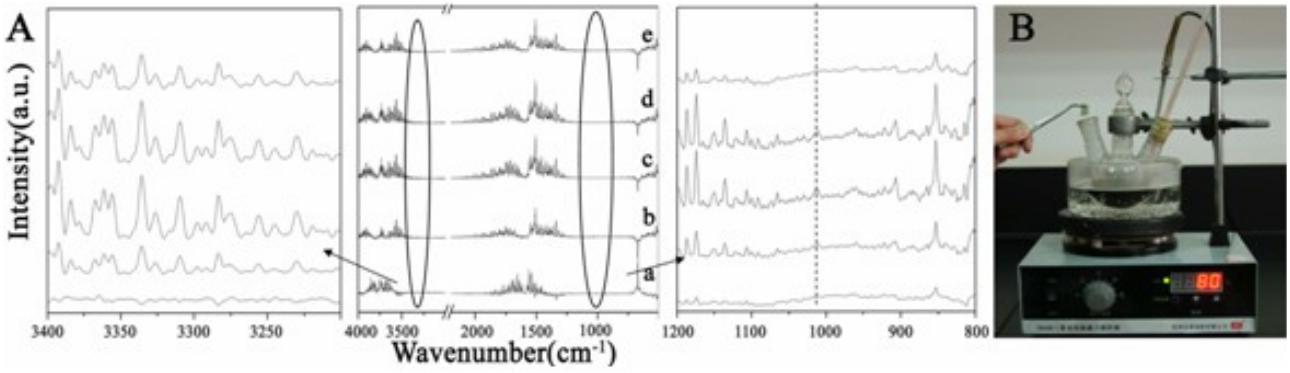

Fig. S11 A) Evolution with the temperature of the FT-IR spectra of the gases evolved in the thermal pyrolysis of Fe_3O_4 NPs stabilized by OA and ammonia: a-e) 55 □, 80 □, 140 □, 155 □ and 180 □, respectively; B) the picture of NH_3 gas released from Fe_3O_4 NPs stabilized by OA and ammonia.

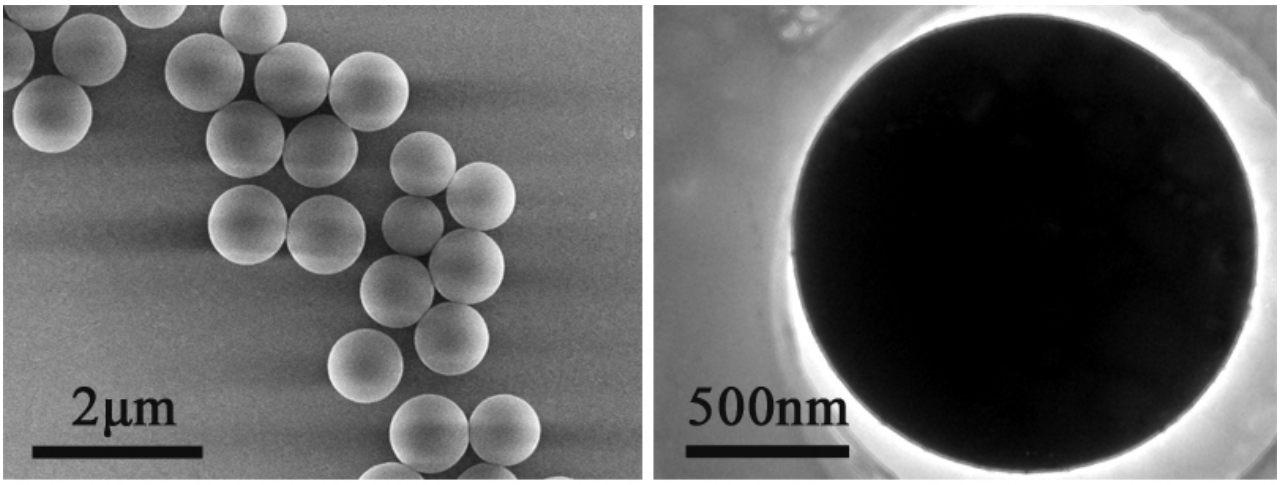

Fig. S12 Typical SEM and TEM images of microspheres prepared without ammonia.

4.2 Effect of OA on the formation of HMGSs

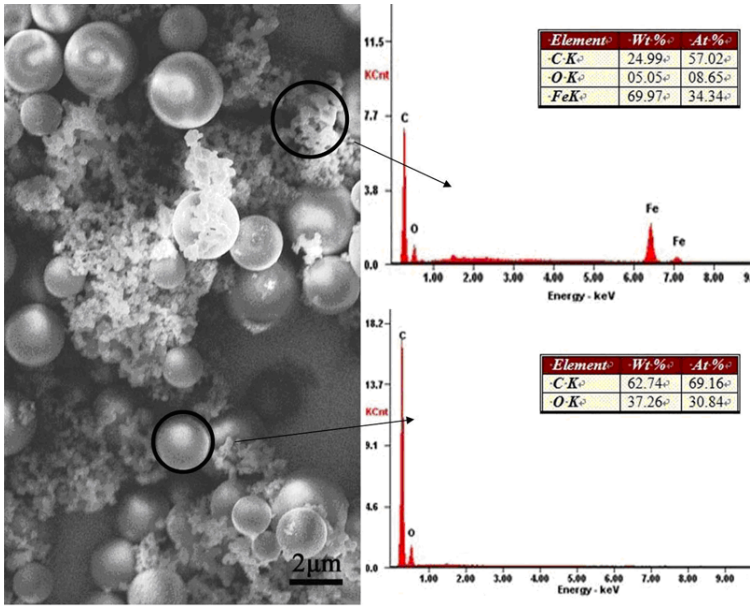

Fig. S13 Typical SEM image of microspheres prepared without OA; EDX spectra show the chemical composition of the areas labeled by the black circles, respectively.

5 Magnetics and adsorption properties of HMGSs

In fact, it is an undeniable that carbon shell could weaken the magnetic response of HMGSs as shown in the field-dependent magnetization curve (Fig. S14). The magnetization saturation (*Ms*) value is about 22.34 emu g^{-1}. Taking into account that the sample contains 49.7 wt% Fe_3O_4, it gives a value of 44.95 emu g^{-1}, which is much lower than that of similarly sized NPs prepared by other methods (85 emu g^{-1}).[9] The low magnetization saturation (*Ms*) value and a small hysteresis loop appear, suggesting that HMGSs have ferromagnetic behavior. These are maybe attribute to the surface spin canting effects and the surfactant coating reducing the total magnetic moment of the Fe_3O_4 NPs,[10, 11] and conversion of part of Fe_3O_4 to Fe_2O_3 during high temperature carbonization. In experiment, however, HMGSs floating on the surface of water still could be fast separated under an external magnetic field and can be readily re-dispersed in water by stirring or sonication due to the low coercive force (about 216 Oe), implying the promising application in the treatment of pollutant on the surface of water with the magnetic-assist separation.

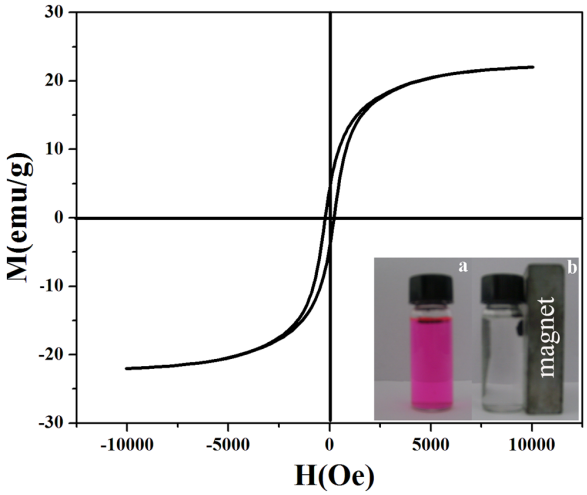

Fig. S14 Magnetization curve measured at 300 K for HMGSs (inset: magnetic-assisted separation of HMGSs after adsorbing RhB).

The HMGSs (~50 mg) were dispersed and sonicated in 10 mg L^{-1} aqueous Cu^{2+}, Cd^{2+}, As^{3+}, Ag^{+} and Au^{3+} ions for 4 h, respectively. The adsorption capacities Q (mg g^{-1}) were obtained as follows: $Q = [(C_1-C_2)V]/m$; where C_1 and C_2 denote the initial and final concentrations (mg g^{-1}) of metal ion in the aqueous solution, respectively, V is the volume of metal ion solution and m is the weight of the adsorbent.[12]

Table S2 Adsorption capacity of HMGSs for metal ions.

Metal ions	Cu^{2+}	Cd^{2+}	Ag^{+}	Au^{3+}	As^{3+}
Adsorption capacity (mg g^{-1})	1.4564	1.4062	1.2036	1.762	2.2112

6 Synthesis and application of HMGS@TiO_2

Due to the moderate synthesis conditions, the compact TiO_2 NP layer about 10-20 nm rather than a TiO_2 film disperse uniformly on the surface of HMGSs, resulting in slightly increasing of the surface roughness (shown in Fig. S15). Meanwhile, energy dispersive X-ray analysis of the obtained spheres reveals the existence of C, Ti, and O elements. The lattice fringes corresponding to (101) (d_{101} = 0.35 nm) crystallographical planes of anatase TiO_2 are clearly observed in HRTEM (Fig. S15C and Fig. S15D).

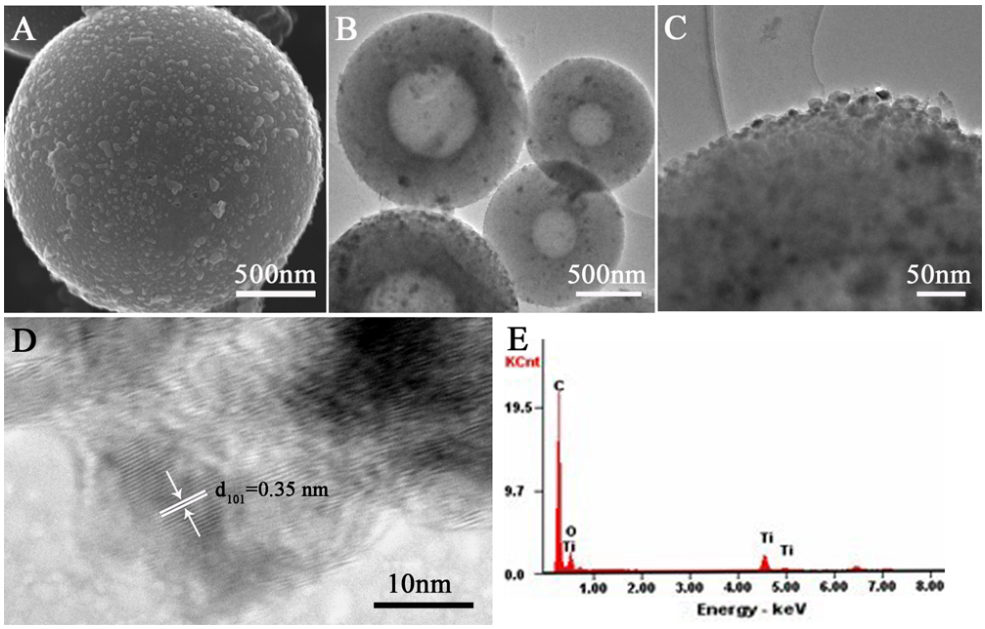

Fig. S15 Typical SEM (A), TEM images (B and C) and EDX spectra (E) of HMGS@TiO_2 microspheres, (D) HRTEM images of TiO_2 NPs.

Table S3 Phosphopeptides ion peaks observed in the MALDI mass spectrum of tryptic digests of α-casein and β-casein.

NO.	phosphopeptide sequences	Number of phosphorylation sites	$[M+H]^+$
β1	FQ[pS]EEQQQTEDELQDK	1	2061.48
β2	FQ[pS]EEQQQTEDELQDKIHPF	1	2556.67
β3	RELEELNVPGEIVE[pS]L[pS][pS][pS]EESITR	4	3122.55
α1	TVDME[pS]TEVF	1	1237.93
α2	TVDME[pS]TEVFTK	1	1467.47
α3	TVD[Mo]E[pS]TEVFTK	1	1483.33
α4	EQL[pS]T[pS]EENSKK	2	1562.22*
α5	TVDME[pS]TEVFTKK	1	1595.41
α6	VPQLEIVPN[pS]AEER	1	1661.17
α7	YKVPQLEIVPN[pS]AEER	1	1832.64
α8	DIG[pS]E[pS]TEDQAMETIK	2	1927.72
α9	DIG[pS]E[pS]TEDQA[Mo]EDIK	2	1943.68
α10	YKVPQLEIVPN[pS]AEER	1	1951.94
α11	NTMEHV[pS] [pS] [pS]EESII[pS]QETYK	4	2618.54
α12	VNEL[pS]KDIG[pS]E[pS]TEDQAMEDIK	3	2678.34
α13	LRLKKYKVPQLEIVPN[pS]AEERL	1	2704.22

α14	QMEAE[pS]I[pS][pS][pS]EEIVPNPN[pS]VEQK	5	2720.96
α15	Q[Mo]EAE[pS]I[pS][pS][pS]EEIVPNPN[pS]VEQK	5	2737.10
α16	NTMEHV[pS][pS][pS]EE[pS]SQETYKQ	4	2746.69
α17	KEKVNEL[pS]KDIG[pS]E[pS]TEDQAMEDIKQ	3	2935.01
α18	NANEEEYSIG[pS][pS][pS]EE[pS]AEVATEEVK	4	3008.21
α19	NANEEEY[pS]IG[pS][pS][pS]EE[pS]AEVATEEVK	5	3087.38

*[M+Na]+

Reference

1 Z. Wang, H. Guo, Y. Yu and N. He, *J. Magn. Magn. Mater.*, 2006, **302**, 397.

2 Y. Hou, H. Kondoh, M. Shimojo, E. O. Sako, N. Ozaki, T. Kogure and T. Ohta, *J Phys. Chem. B*, 2005, **109**, 4845.

3 Y. Wang, J. F. Wong, X. Teng, X. Z. Lin and H. Yang, *Nano Lett.*, 2003, **3**, 1555.

4 C. Yao, Y. Shin, L. Q. Wang, C. F. Windisch, W. D. Samuels, B. W. Arey, C. Wang, W. M. Risen and G. J. Exarhos, *J. Phys. Chem. C*, 2007, **111**, 15141.

5 M. Zheng, Y. Liu, Y. Xiao, Y. Zhu, Q. Guan, D. Yuan and J. Zhang, *J. Phys. Chem. C*, 2009, **113**, 8455.

6 X. Sun and Y. Li, *J. Colloid Interface Sci.*, 2005**, 291**, 7.

7 X. Jia, D. Chen, X. Jiao and S. Zhai, *Chem. Commun.*, 2009, **8**, 968.

8 E. D. Obraztsova, M. Fujii, S. Hayashi, V. L. Kuznetsov, Y. V. Butenko and A. L. Chuvilin, *Carbon*, 1998, **36**, 821.

9 P. G. Wu, J. H. Zhu and Z. H. Xu, *Adv. Funct. Mater.*, 2004, **14**, 345.

10 Y. Ma, Z. Hu, L. Yu, Y. Hu, B. Yue, X. Wang and Y. Chen, *J. Phys. Chem. B*, 2006, **110**, 20118.

11 S. V. Pol, V. G. Pol, A. Gedanken, I. Felner, M-G Sung and S. Asai, *Inorg. Chem.*, 2007, **46**, 4951.

12 M. Bystrzejewski, K. Pyrzyńska, A. Huczko and H. Lange, *Carbon*, 2009, **47**, 1189.